

THERMAL EMISSION OF EXOPLANET XO-1B

PAVEL MACHALEK^{1,2}, PETER R. MCCULLOUGH², CHRISTOPHER J. BURKE², JEFF A. VALENTI², ADAM BURROWS³,
JOSEPH L. HORA⁴

Accepted for publication in The Astrophysical Journal

ABSTRACT

We estimate flux ratios of the extrasolar planet XO-1b to its host star XO-1 at 3.6, 4.5, 5.8 and 8.0 microns with the IRAC on the *Spitzer Space Telescope* to be 0.00086 ± 0.00007 , 0.00122 ± 0.00009 , 0.00261 ± 0.00031 and 0.00210 ± 0.00029 , respectively. The fluxes are inconsistent with a canonical cloudless model for the thermal emission from a planet and suggest an atmosphere with a thermal inversion layer and a possible stratospheric absorber. A newly emerging correlation between the presence of a thermal inversion layer in the planetary atmosphere and stellar insolation of the planet (Burrows et al. 2007b) is refined. The sub-stellar point flux from the parent star at XO-1b of $\sim 0.49 \times 10^9 \text{ erg cm}^{-2} \text{ s}^{-1}$ sets a new lower limit for the occurrence of a thermal inversion in a planetary atmosphere.

Subject headings: stars:individual(XO-1) — binaries:eclipsing — infrared:stars — planetary systems

1. INTRODUCTION

Over 270 extrasolar planets have been reported, more than 30 of which transit their primary star⁵. In addition to the mass, radius and inclination of the planet evident from transits, atmospheric composition can also be studied through transmission spectroscopy, leading to detections of sodium, water and methane (Charbonneau et al. 2002; Tinetti et al. 2007; Swain et al. 2008). In addition, secondary eclipse observations provide broadband emission spectra (Knutson et al. 2008; Charbonneau et al. 2008), planetary brightness temperatures (Charbonneau et al. 2005; Deming et al. 2005; Harrington et al. 2007) and even day-night temperature contrast (Knutson et al. 2007). Torres et al. (2008) provide a reanalysis of light curves and RV measurements of all then known transiting planets.

For “hot Jupiters”, planets with $P_{orb} \lesssim 10$ days, a favorable planet-star ratio in the IR allows for direct detection of the planetary atmosphere by comparing the combined flux from the star and the planet during and out of secondary eclipse at the superior conjunction. The contrast ratio in the mid-IR (1-10 microns) can be higher than 10^{-3} (cf. observations of HD 189733b by Charbonneau et al. (2008)) and theoretical predictions by Burrows et al. (2006), Fortney et al. (2006) and Burrows et al. (2007a), allowing for detection of fluxes from planets at secondary eclipse using the IRAC, IRS, and MIPS cameras of the *Spitzer Space Telescope* (Werner et al. (2004)). Five planets have had their secondary eclipse fluxes measured in one

or more IRAC bands: TrES-1 (Charbonneau et al. 2005), HD 209458b (Deming et al. 2005; Knutson et al. 2008), HD 189733b (Knutson et al. 2007), HD 149026b (Harrington et al. 2007) and GJ 436b (Deming et al. 2007). In addition low resolution spectra of 2 transiting planets were obtained with the IRS spectrometer between ~ 7 and $15 \mu\text{m}$: HD 189733b (Grillmair et al. 2007) and HD 209458b (Richardson et al. 2007).

Recently a detection of an atmospheric feature attributed to water has been claimed by Tinetti et al. (2007) and Barman (2007) by studying the transit flux ratios of HD 189733b and HD 209458b, respectively. Burrows et al. (2007a) analyzed the secondary transmission spectra of HD 209458b at all 4 infrared IRAC *Spitzer* channels observed by Knutson et al. (2008) and suggested the observations are consistent with an atmospheric thermal inversion layer and yet unknown stratospheric absorber. A detailed study of the IR secondary eclipse planetary spectra of HD 209458b, HD 189733b, TrES-1, HD 149026b and non-eclipsing HD 179949b, and *v* And b by Burrows et al. (2007b) suggests that the presence of such a stratospheric absorber might be dependent on the flux from the star at the sub-stellar point on the planet as well as second order effects like metallicity and planetary surface gravity. In the Burrows et al. (2007b) interpretation planets with high sub-stellar point flux (e.g., HD 209458b, OGLE-Tr-56b, OGLE-Tr-132b, TrES-2b and XO-3b) would have a stratospheric layer and a water feature in emission while planets with lower fluxes (XO-1b, TrES-1, XO-2b and HD 189733b) would have no such layer and a water feature in absorption. Fortney et al. (2007) also suggest a similar division of planetary spectra based on incident stellar flux. Based on the planetary sub-stellar point flux from the star, both Burrows et al. (2007b) and Fortney et al. (2007) predict that XO-1b should not exhibit a thermal inversion in its atmosphere.

We present observations of the infrared spectral energy distribution (SED) of the planet XO-

Electronic address: pavel@jhu.edu

¹ Department of Physics and Astronomy, Johns Hopkins University, 3400 North Charles St., Baltimore MD 21218

² Space Telescope Science Institute, 3700 San Martin Dr., Baltimore MD 21218

³ Department of Astrophysical Sciences, Princeton University, Princeton, NJ 08544

⁴ Harvard-Smithsonian Center for Astrophysics, 60 Garden St., MS-65, Cambridge, MA 02138

⁵ <http://www.inscience.ch/transits/>

1b (McCullough et al. 2006) in all 4 IRAC channels obtained during secondary eclipses with the IRAC of *Spitzer Space Telescope*. By comparing our $\sim 4\text{--}8\ \mu\text{m}$ SED with atmospheric models, we test for the presence of a thermal inversion layer in XO-1b.

2. OBSERVATIONS

The InfraRed Array Camera (IRAC; Fazio et al. 2004) has a field of view of $5.2' \times 5.2'$ in each of its four bands. Two adjacent fields are imaged in pairs (3.6 and 5.8 microns; 4.5 and 8.0 microns). The detector arrays each measure 256×256 pixels, with a pixel size of approximately $1.22'' \times 1.22''$. We have observed XO-1 in all 4 channels in two separate Astronomical Observing Requests (AORs) in two different sessions: the 4.5 and 8.0 micron channels for 5.9 hours on UT 2007 April 02 (AOR 21374464) and the 3.6 and 5.8 micron channels for 5.9 hours on UT 2007 Aug 10 (AOR 21374208). We used the 12 s frame time, obtaining 1620 full-array images in each bandpass with a cadence of 13.2 s and an effective integration time of 10.4 s. The pointing was not dithered and was selected such that for the Apr 2007 observations in the 4.5 and 8.0 micron channels, two bright calibrators for XO-1 (2MASS J16021184+2810105 J=9.939 J-K=0.412) were used: 2MASS J16021795+2813328: J = 9.913 J - K = 0.564 and 2MASS J16020133+2809268: J = 12.542 J - K = 0.795. The Aug 2007 observations in the 3.6 and 5.8 micron channels used 2 bright calibrators: 2MASS J16021311+2809004: J=11.045 J - K = 0.652 and 2MASS J16020133+2809268: J = 12.542 J - K = 0.795.

We used the standard IRAC Basic Calibrated Data products (version 16.1) described in the Spitzer Data Handbook⁶, which includes dark frame subtraction, multiplexer bleed correction, detector linearization, and flat-fielding of the images. We converted the times recorded by the spacecraft in the FITS file header keyword DATE-OBS to heliocentric Julian dates using the orbital ephemeris of the spacecraft provided by the Horizons Ephemeris System⁷.

Prior to performing aperture photometry, we resampled the images in all four channels to a 10 times finer grid in each spatial direction using flux-conserving bilinear interpolation (similar to Harrington et al. (2007)). With the implementation for aperture photometry that we used, resampling makes a marginal improvement in the photometry, i.e. a slightly lower r.m.s. of out-of-eclipse points, presumably related to how the routine handles fractional pixels at the edge of the aperture.

The zodiacal background was subtracted in each channel by constructing a histogram of all pixels in each image and fitting a Gaussian to the distribution of the zodiacal background brightness. A constant mean value of the Gaussian was then subtracted from each pixel in the image to construct a background-subtracted image. The centroids of XO-1 and the 2 calibrators were evaluated by fitting a Gaussian to the stellar flux distribution. The pointing varied by 0.3 pixel, and the shifting of the stellar centroid within a pixel, which have sub-pixel sensitivity variations, resulted in a modulation of the stellar flux in the 3.6 and 4.5 micron channels (described below).

Aperture photometry was then performed on the images with an aperture radius of 4 pixels, which was found to be the optimum value for all 4 channels. The size of the aperture was determined by minimizing the rms scatter in the light curve for observations outside of the eclipse. Apertures smaller than 4 pixels contained insufficient stellar flux and larger apertures were more contaminated by the sky (especially in the high background signal of the 5.8 and 8.0 micron channels). An appropriate aperture correction for each channel was applied to the stellar flux value according to the Spitzer Data Handbook of [1.112, 1.113, 1.125, 1.218] for the [3.6; 4.5; 5.8 and 8.0] micron channels, respectively. The σ of the out-of-eclipse points was calculated iteratively using 3- σ outlier rejection at each step until no more points were rejected. To remove cosmic rays the resultant robust σ was used to reject entire images which contain the 3- σ outliers above and below the mean of the light curve. 1.4%; 1.9%; 3.0 %, 2.4 % of images from the 3.6, 4.5, 5.8 and 8.0 micron channels, respectively, were removed in this fashion. The higher rejection rate in the two redder channels is consistent with a higher number of cosmic ray-affected pixels in these channels (Patten et al. 2004). Throughout the analysis we have preserved flux units.

2.1. 3.6 and 4.5 micron time series

The 3.6- μm time series exhibited a sharp increase during the first ~ 30 minutes of exposure for XO-1 and the 2 calibrators, presumably as a result of the instrument reaching a new equilibrium after previous observations. Such relaxation effects can reach several percent and usually stabilize within the first hour of observations of a new target. We have ignored the first 125 points (~ 30 min) in the 3.6- μm time series in addition to the high-sigma outlier rejection as described in the previous section.

A strong correlation between the sub-pixel centroid and stellar brightness was observed in both the 3.6- μm and 4.5- μm channels, with flux magnitudes of $\sim 0.6\%$ and 0.8% , respectively. This well studied effect (Charbonneau et al. 2005; Morales-Calderón et al. 2006) is due to the InSb detector intrapixel sensitivity variations as the spacecraft jitters ~ 0.3 arcsec in orientation over a period of ~ 3000 seconds⁸. The uncorrected sub-pixel intensity variations are clearly visible in the time series of XO-1 in the 3.6- μm and 4.5- μm channels in Fig. 1. We have corrected for this sub-pixel intensity variations after Charbonneau et al. (2008) by fitting a quadratic function to the photometric flux points of XO-1b observed out-of-eclipse as a function of the x and y sub-pixel centroids:

$$I_{\text{subpixel}} = b_1 + b_2 \times x + b_3 \times x^2 + b_4 \times y + b_5 \times y^2, \quad (1)$$

where x and y are the subpixel centroids of center of light of the star and b_n are the fit parameters. The rms residual of the XO-1 time series for points outside of the eclipse after correction for the sub-pixel intensity variation was 0.0020, which is 18% higher than a theoretical estimate of XO-1 Poisson noise based on detector

⁶ <http://ssc.spitzer.caltech.edu/irac/dh/>

⁷ <http://ssd.jpl.nasa.gov/>

⁸ <http://ssc.spitzer.caltech.edu/documents/exoplanetmemo.txt>

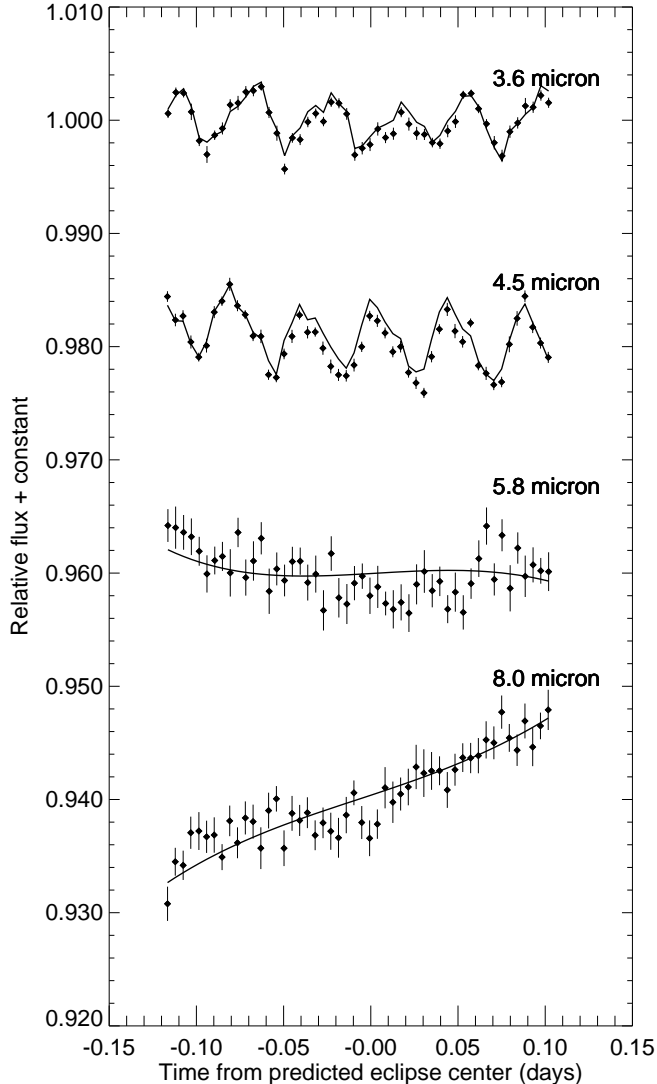


Fig. 1.— Secondary eclipse observations of XO-1b with IRAC on *Spitzer Space Telescope* obtained on UT 2007 April 02 and UT 2007 Aug 10 in 3.6, 4.5, 5.8 and 8.0 micron channels (from top to bottom) binned in 6-minute interval and normalized to 1 and offset by 0.02 for clarity. The overplotted solid lines do *not* represent a fit to the data, but rather show the correction for the detector effects. The 3.6 and 4.6 micron time series are decorrelated using XO-1 out-of-eclipse points and the 5.8 and 8.0 micron time series is detrended using a fit to a calibrator star in the field (see §2.1 & §2.2 for details.)

read noise and background noise. The time series was then normalized by taking the robust average of out-of-eclipse points and binned in 6-minute intervals containing approximately 30 individual measurements each (see Fig. 2).

The 4.5- μm time series also exhibited an initial relaxation-induced brightness increase and consequently 139 points corresponding to the first ~ 30 minutes of observations were rejected, which is more points than in the 3.6- μm time series. The analysis of the time series was identical to that of the 3.6- μm time series. The rms of out-of-eclipse points was 0.0024, which is 19% higher

TABLE 1
XO-1 ABSOLUTE FLUXES

IRAC channel effective λ (microns)	XO-1 flux (mJy)	XO-1 instrumental magnitude (mag)
3.6	45.1 ± 2.3	9.49
4.5	28.5 ± 1.4	9.50
5.8	18.1 ± 0.9	9.51
8.0	11.7 ± 0.6	9.35

than the theoretical estimate and is similar to that of TrES-1 (rms=0.0027 Charbonneau et al. (2005)).

We have tested for the linearity of the detector response in the 3.6 and 4.5 micron channels in which XO-1 is close to the onset of detector non-linear response. Using a subset of data from the SAGE survey (Meixner et al. 2006) obtained in the high dynamic range (HDR) mode of IRAC camera with both 0.6s and 12.0s integration times we are able to determine that both the 3.6 micron and 4.5 micron XO-1 fluxes are unsaturated and in the detector linear regime response. Table 1 shows the absolute XO-1 fluxes and the instrumental magnitudes in the four IRAC channels.

2.2. 5.8 and 8.0 micron time series

The 5.8 and 8.0 micron time series were recorded with Si:As detectors and do not thus exhibit the prominent sub-pixel intensity variations evident in the 3.6 micron and 4.5 micron channels. The first ~ 30 minutes of observations (139 data points) were rejected as the instrument settled into a new equilibrium state. Fig. 1 shows intensity variation with time, which is caused by changes in the effective gain of individual pixels over time. This effect has also been observed by Harrington et al. (2007) at 8 micron with IRAC and by Deming et al. (2006) at 16 micron with IRS. The intensity variations are dependent on the illumination level of the individual pixel (Knutson et al. 2007, 2008), pixels with high illumination will reach their equilibrium within ~ 1 hour, but lower illumination pixels increase in intensity over time, approximately proportional to the inverse of the logarithm of illumination. We have decided not to correct each pixel in the image as Knutson et al. (2007) have done in their 33-hour observation of HD 189733 in the 8 micron channel of IRAC and instead fit a combined linear and quadratic logarithm function of time from the beginning of observations to the time series of the bright calibrator 2MASS 16020133+2809268. The fit to the time series of the calibrator was then used to remove the detector ramp from the time series of XO-1 as depicted in Fig. 1:

$$I_{model} = a_1 + a_2 \times \Delta t + a_3 \times \ln \Delta t + a_4 \times (\ln \Delta t)^2, \quad (2)$$

where I_{model} is the model flux, Δt is the time since the beginning of observations and a_i are the free parameters. The detector ramp intensity decreased in flux during the 5 hours of observation by $\sim 0.2\%$, following a similar trend seen by Knutson et al. (2008) in their 5.8 micron time series of brighter HD 209458b. After removal of the detector ramp and normalization, the rms of unbinned 5.8 micron out-of-eclipse points for XO-1 was 0.0081,

which is 44% higher than theoretical Poisson noise, based on detector read noise and background noise.⁹ The normalized and binned 5.8 micron time series is depicted in Fig. 2.

Fitting the detector ramp using a calibrator star, which is non-variable at the 0.012 level after detector ramp removal, allows us to bypass using XO-1 itself to remove the detector ramp by making a fit to its 5.8 micron out-of-eclipse points. The choice whether to correct for the detector ramp of XO-1 using the photometry of a calibrator star or the target star itself could be a limiting factor in our analysis. Deming (2008, p.c.) has indicated that in a long (> 10 hours) series of full-frame 12s-exposure IRAC photometry, fitting the detector ramp to the target star while masking out the points in the eclipse could be more appropriate. We implemented each of the two alternate methods of correction, and for these observations of XO-1b, the measured depths at 5.8 micron are within 1- σ of each other.

Charbonneau et al. (2005), Knutson et al. (2007), Harrington et al. (2007) and Deming et al. (2007) have reported a nonlinear flux increase over time in the 8.0 micron IRAC channel. We also detect a nonlinear increase in the brightness of XO-1 and in the 2 calibrators, in addition to the sharp increase during the first ~30 minutes of observations (137 points). The initial ramp-up data were discarded and the ~ 1.6% non-linear increase of the XO-1 time series over 5 hours (see Fig. 1) was removed by fitting a combined linear and quadratic logarithm function (eq. 2) to the time series of the first calibrator 2MASS J16021795+2813328 and dividing the XO-1 time series by the fit. The time series was normalized using out-of-eclipse points and binned into 6-minute bins (Fig. 2) for viewing clarity. The resulting rms of unbinned out-of-eclipse points for the XO-1 time series was 0.0075, 74% above Poisson noise, but similar to that of TrES-1 (rms = 0.0085, (Charbonneau et al. 2005)).

3. ANALYSIS

We fit the secondary eclipse light curves using the formalism of Mandel & Agol (2002) with no stellar limb darkening and adopt stellar and orbital parameters (Holman et al. 2006)¹⁰: $R_\star = 0.928^{+0.018}_{-0.013} R_\odot$, $R_p = 1.184^{+0.028}_{-0.018} R_{Jup}$ ¹¹, $i = 89.31^{+0.46}_{-0.53}$ degrees, and $a = 0.0488 \pm 0.0005$ AU with ephemeris (McCullough et al. 2006)

$$T_c(E) = 2,453,808.9170(HJD) + E(3.941534 \text{ days}). \quad (3)$$

We fit the depth of the eclipse ΔF and the timing of the centroid ΔT independently in all 4 channels in the unbinned light series using Levenberg-Marquardt minimization (Press et al. 1992) with an equal error assigned to all points, which is equal to the rms of out-of-eclipse points in each time series. Best-fit eclipse curves are plotted in Fig. 2 and the eclipse parameters are listed in Table 2. They are the channel wavelength, eclipse depth

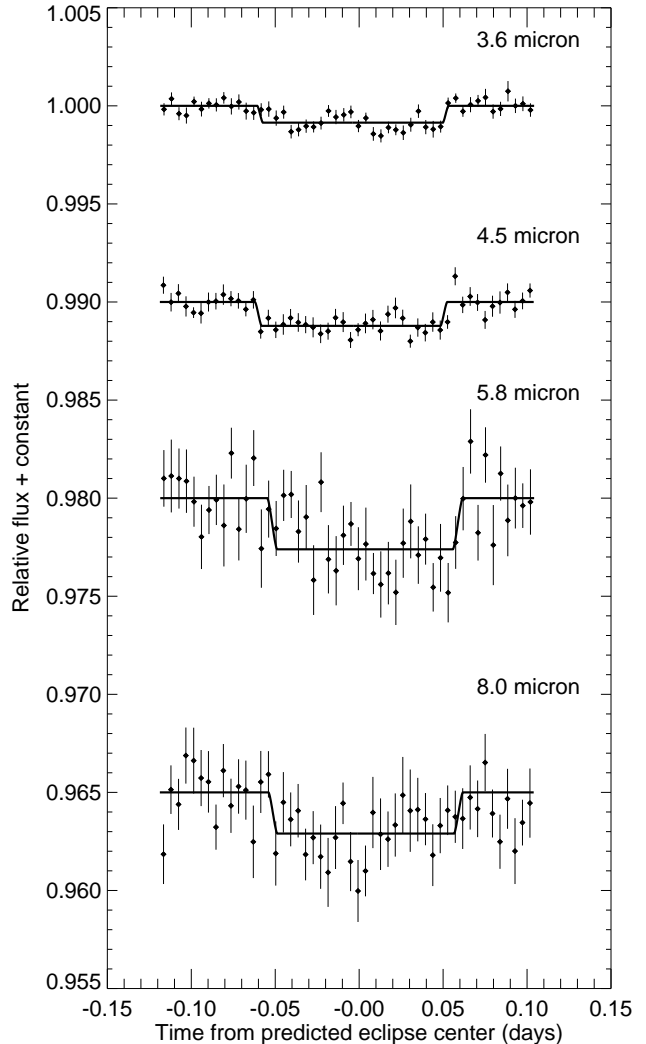


FIG. 2.— Secondary eclipse of XO-1b observed with IRAC on *Spitzer Space Telescope* in 3.6, 4.5, 5.8, and 8.0 micron channels (top to bottom) corrected for detector effects, normalized and binned in 6-minute intervals and offset for clarity. The best-fit eclipse curves are overplotted.

ΔF , eclipse mid-center time in HJD, and the timing offset Δt in minutes from the expected secondary eclipse mid-center time for an assumed eccentricity of zero, and the reduced χ^2 . The reduced χ^2 is close to 1.0 in all 4 channels, indicating a good fit to the data.

To estimate the errors on the depth and mid-eclipse timing we performed the error analysis using the bootstrap method from Press et al. (1992). The bootstrap method makes no prior assumptions about the distribution of the noise in the data and the data points are not altered as in the Monte-Carlo analysis. For 10,000 trial runs we have randomly drawn with replacement points from the normalized- and detector-effect-decorrelated, but otherwise unaltered, light curve, until we had the same number of data points in the light curve that we started with. During each iteration we performed the full eclipse fitting for eclipse depth ΔF and eclipse mid-center ΔT . The 1- σ errors for ΔF and ΔT were computed by fitting a Gaussian to the respective 1-D distribution of bootstrap points and are reported in Table 2.

⁹ http://ssc.spitzer.caltech.edu/documents/irac_memo.txt

¹⁰ We have also reduced the data using the stellar and orbital parameters from Torres et al. (2008) as a test, but the eclipse depths changed negligibly and eclipse mid-center timings were all within 1- σ .

¹¹ $1 R_{Jup} = 71,492$ km.

TABLE 2
SECONDARY ECLIPSE BEST FIT PARAMETERS

λ (microns)	Eclipse Depth ΔF	Eclipse Center Time (HJD)	Time offset ΔT (min)	Reduced χ^2
3.6	0.00086 ± 0.00007	$2454323.28342 \pm 0.00242$	-5.42 ± 3.49	0.76
4.5	0.00122 ± 0.00009	$2454193.21175 \pm 0.00259$	-6.94 ± 3.72	0.84
5.8	0.00261 ± 0.00031	$2454323.29066 \pm 0.00488$	5.00 ± 7.03	0.89
8.0	0.00210 ± 0.00029	$2454193.22043 \pm 0.00486$	5.56 ± 7.00	0.99

The eclipse depth errors $\Delta F = [0.00007, 0.00009, 0.00031, 0.00029]$ for the $J = 9.939$ XO-1 compare favorably with the eclipse depth errors $[0.00009, 0.00015, 0.00043, 0.00026]$ of Knutson et al. (2008) for the $J = 6.591$ HD 209458, despite the fact that XO-1 is dimmer. XO-1 observations were made in the full-array mode with 10.4-s integration time and readout time 2.8 s for a total of 1,620 images, while the HD 209458 observations were made in sub-array mode with exposure time of 0.1 s in sets of 64 in each channel totaling 26,880 usable images. The S/N scales as $\propto \sqrt{n_{exp}} * f_e * \Delta t / \sigma_{total}$, where n_{exp} is the number of exposures during the duration of the eclipse, f_e is the stellar flux in signal electrons, Δt is the integration time and σ_{total} is the combined Poisson, readout and background noise. The predicted eclipse depth errors for XO-1 in the four IRAC channels are then $[0.4; 0.5; 0.9; 2.5]$ times the respective eclipse depth errors for the 21 times brighter HD 209458.

To test the robustness of our data reduction and analysis technique and consistency with other observations in the IRAC full-array mode we have re-reduced the 4.5 and 8.0 micron IRAC secondary eclipse data of TrES-1 by Charbonneau et al. (2005) with our pipeline, rejecting the first 30 minutes in both channels. The procedure described in §2.1 and §2.2 was used together with updated stellar and planetary parameters of Torres et al. (2008) to derive the eclipse depths relative to the star TrES-1 of $\Delta F_{4.5\mu m} = 0.00043$ and $\Delta F_{8.0\mu m} = 0.00194$, which are -1.1σ and -0.9σ away from the Charbonneau et al. (2005) secondary eclipse depths of $\Delta F_{4.5\mu m} = 0.00057 \pm 0.00013$ and $\Delta F_{8.0\mu m} = 0.00225 \pm 0.00036$, respectively. Our secondary eclipse [4.5; 8.0]micron channel mid-center timing offsets of $[+12.5; -2.3]$ minutes are $[-1.1\sigma; -2.0\sigma]$ away from the Charbonneau et al. (2005) [4.5; 8.0]micron channel values $+19.6 \pm 6.6$ min and $+8.3 \pm 5.2$ minutes, respectively. While the eclipse depths are consistent at the $\sim 1\text{-}\sigma$ level, the eclipse mid-center timing offset in the 8.0 micron channel is only mildly consistent at the 2.0σ level, probably because Charbonneau et al. (2005) observations were made using multiple Astronomical Observation Requests (AORs) which resulted in arbitrary flux shifts in the time series. Charbonneau et al. (2005) do not mention how they have corrected for these flux shifts. Despite this fact our pipeline is capable of reproducing their results to within $\sim 1\text{-}\sigma$ in eclipse depth and $\sim 2\text{-}\sigma$ in mid-eclipse timing. We have thus demonstrated that our reduction pipeline is robust and the secondary eclipse depth estimates are consistent with other major full-array pipelines.

4. DISCUSSION

The eclipse mid-center timings for XO-1b in Table 2 are individually consistent with zero timing residuals for a circular orbit based on the ephemeris by McCullough et al. (2006), but the April and August 2007 combined timings show a time shift. The UT Apr 2 2007 observations of 4.5 micron and 8.0 micron channels have a combined eclipse mid-center timing of $2454193.21366 \pm 0.00228$ HJD, with a delay of -4.2 ± 3.3 min, while the UT 2007 Aug 10 observations of 3.6 micron and 5.8 micron channels have a combined center of eclipse time of $2454323.28485 \pm 0.00217$ HJD, with a delay of -3.4 ± 3.1 min. The mid-eclipse timing offsets can be interpreted as evidence for further planets in the system, as can a non-uniform brightness distribution of the planet (which can change the shape of eclipse ingress and egress and, thus, shift the eclipse mid-center time (Williams et al. 2006)), or as evidence for a non-zero eccentricity. Using the larger mid-eclipse April time offset, the approximate equation (e.g. Kopal (1959) Eq. 9-23)

$$e \times \cos(\omega) \simeq \frac{\pi \Delta t}{2P}, \quad (4)$$

where e is the eccentricity, ω is the longitude of periastron, P is the orbital period, and Δt is the centroid time shift from expected time of secondary eclipse, allows us to set a 2σ upper limit on $e \times \cos(\omega) < 0.0024$.

The XO-1b eclipse depths in Fig. 3 show several trends. The planet-to-star contrast of XO-1b peaks in the 5.8 μm channel, with a decrease in the 3.6 micron and 4.5 micron channel and a slight decrease towards the 8.0 micron channel. Furthermore the flux in the 4.5 μm channel is higher than in the 3.6 micron channel, which does not match the general character of the cloudless models of Burrows et al. (2006) for redistribution parameter $P_n = 0.3$ (dot-dashed line and open circles for band-averaged ratios in Fig. 3), which predict a lower flux at 4.5 microns than at 3.6 microns; the model with thermal inversion predicts the opposite. Since the observations manifest a higher flux in the 4.5 micron channel than at 3.5 micron, a thermal inversion in the atmosphere might be indicated. $P_n = 0$ corresponds to no heat redistribution from the planetary day-side to the night-side and $P_n = 0.5$ stands for full redistribution (see Burrows et al. (2007b) for details). The possibility of thermal inversion in a planetary atmosphere has been suggested by Hubeny et al. (2003), Burrows et al. (2006, 2007a) and Fortney et al. (2007). Recently, Burrows et al. (2007a,b) suggested that model spectra could match the observations of HD 209458b and HD 149026b if a stratospheric absorber of unknown composition (possibly tholins, polyacetylenes, TiO or

VO) were present in the atmosphere of the planet. The presence of a stratospheric absorber would yield a thermal inversion in the planetary atmosphere and the presence of the water features in emission for a variety of heat redistribution parameters P_n .

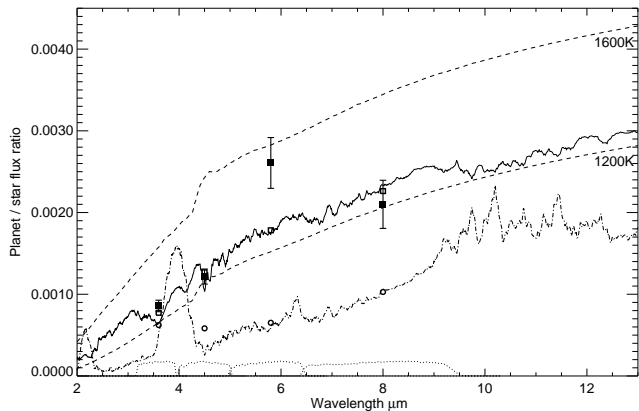


FIG. 3.— *Spitzer Space Telescope* IRAC secondary eclipse depths for XO-1b with bootstrap error bars (filled squares). The predicted emission spectrum of the planet with an upper atmospheric absorber of $\kappa_e = 0.1 \text{ cm}^2/\text{g}$ and a redistribution parameter of $P_n=0.3$ is plotted as a solid line. A model with no atmospheric absorber and a redistribution parameter of $P_n=0.3$ is over plotted with dot-dashed line (see §3 for details). The band-averaged flux ratios are plotted as open squares and open circles for the models with and without stratospheric absorber, respectively. The normalized *Spitzer Space Telescope* IRAC response curves for the 3.6-, 4.5-, 5.8-, and 8.0 micron channels are plotted at the bottom of the figure (dotted lines). The theoretical flux ratios obtained from a XO-1 stellar spectrum (from <http://kurucz.harvard.edu/stars/X01/>) and an assumed black-body spectrum for the planet at [1200, 1600] K are plotted as dashed lines.

Our observations suggest the presence of a thermal inversion layer and a possible stratospheric absorber in the atmosphere of the XO-1b planet. The solid line and open squares in Fig. 3 depict an atmospheric model of XO-1b, following the methodology of Burrows et al. (2006, 2007a) with a thermal inversion and a stratospheric absorber of opacity of $\kappa_e = 0.1 \text{ cm}^2/\text{g}$ and redistribution parameter of $P_n = 0.3$. The latter model fits the data better than the canonical cloudless model with $P_n = 0.3$ (dot-dashed curve and open circles for averaged band ratios). The band-averaged flux ratios for the model with a stratospheric absorber (open squares) are within the error bars for the 3.6, 4.5, and 8.0 micron channels, but are inconsistent by 2.7σ with the band-averaged flux ratios for the 5.8 micron channel. This is similar to the situation for the IRAC fit to the observations by HD 209458b by Knutson et al. (2008). The absorber-free canonical model (dot-dashed line) is clearly inconsistent with our observations (Fig. 3) of XO-1b in all 4 channels by [3.4σ , 7.1σ , 6.3σ , 3.7σ], respectively.

Burrows et al. (2007b) and Fortney et al. (2007) suggested that the presence of the stratospheric absorber might be correlated with the incident flux from the star at the sub-stellar point on the planet, the precise level of which is yet to be refined. The presence of an irradiation-induced stratospheric absorber has been

suggested by Burrows et al. (2007a) for HD 209458b (see our Fig. 4) with a sub-stellar flux of $\sim 1.07 \times 10^9 \text{ erg cm}^{-2} \text{ s}^{-1}$ at a distance $a = 0.045 \text{ AU}$. Interestingly, XO-1b has a lower sub-stellar flux of $\sim 0.49 \times 10^9 \text{ erg cm}^{-2} \text{ s}^{-1}$ and a semi-major axis of $a = 0.0488 \text{ AU}$, but still manifests evidence for a thermal inversion. A recent study of the broadband infrared spectrum of HD 189733b (see our Fig. 4) by Charbonneau et al. (2008) finds no evidence for an atmospheric thermal inversion, despite a similar sub-stellar point flux of $\sim 0.47 \times 10^9 \text{ erg cm}^{-2} \text{ s}^{-1}$ (Burrows et al. 2007b) with a smaller semi-major axis $a = 0.0313 \text{ AU}$. Further study of planetary atmospheres should refine the concept of this sub-stellar flux boundary with respect to the presence/absence of a stratospheric absorber and thermal inversion.

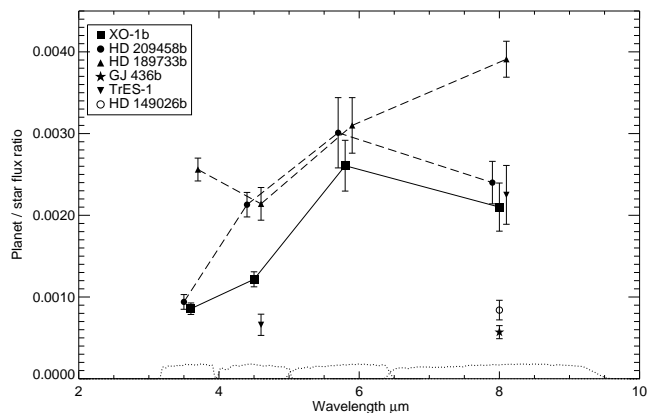


FIG. 4.— Comparison of *Spitzer Space Telescope* IRAC secondary eclipse depths: XO-1b (filled square) from this paper; HD 209458b (filled circle) from Knutson et al. (2008); HD 189733b (filled triangle) from Charbonneau et al. (2008); GJ 436b (filled star) from Deming et al. (2007); TrES-1 (filled upside down triangle) from Charbonneau et al. (2005); and HD 149026b (open circle) from Harrington et al. (2007). The central wavelengths have been offset by [+0.1;-0.1] microns for clarity. The normalized *Spitzer Space Telescope* IRAC response curves for the 3.6-, 4.5-, 5.8-, and 8.0 micron channels are plotted at the bottom of the figure (dotted lines).

Atmospheric water detection has been claimed in the transit broadband spectra of HD 189733b by Tinetti et al. (2007) and in its secondary eclipse spectra by Fortney & Marley (2007). Burrows et al. (2007a) also found evidence for water vapor emission in the atmosphere of HD 209458b. Our data can be interpreted as evidence for rovibrational band of water emission longward of ~ 4.0 microns, which manifests itself as a flux enhancement in Fig. 3 compared to the cloudless model. The depth of the flux ratio trough near the 3.6 micron channel in the atmospheric models with stratospheric absorber strongly depends on the redistribution parameter P_n (Burrows et al. 2007b), especially their Fig. 4). Further modeling would allow tighter constraints on the P_n , not just for XO-1b, but for a variety of planets. The fortuitous importance of the 3.6 micron IRAC channel to the study of planetary atmospheres is likely to be enhanced as the *Spitzer Space Telescope* runs out of cryocoolant in 2009, when only the 3.6 micron and 4.5 micron channels will be available.

5. CONCLUSION

We report the estimated flux ratios of the planet XO-1b in the *Spitzer Space Telescope* IRAC 3.6, 4.5, 5.8 and 8.0- μm channels. We find that the estimated fluxes are not consistent with a canonical cloudless model for thermal emission from the planet and instead may indicate an atmosphere with as yet unknown stratospheric absorber and a likely thermal inversion, which would cause the water band longward of 4.0 microns to switch from absorption to emission. The atmospheric model with a thermal inversion produces a tight match to the data at 3.6, 4.5, and 8.0 microns, but is inconsistent by 2.7σ with observations at 5.8 microns. This is similar to observations of HD 209458b (Knutson et al. 2008).

The presence or absence of the stratospheric absorber and thermal inversion layer has been linked to the flux from the parent star at the sub-stellar point on the planet. The XO-1b sub-stellar point flux of $\sim 0.49 \times 10^9 \text{ erg cm}^{-2} \text{ s}^{-1}$ is the lowest so far reported for a planetary atmosphere with a thermal inversion. Observations of atmospheres of other planets may permit a better understanding of the thermal inversion layer and parametrization of the characteristics that create such a thermal inversion.

The authors would like to thank J. E. Stys, R. Gilliland, C. M. Johns-Krull, and K. A. Janes for helpful discussions. The authors would also like to acknowledge the use of publicly available routines by Eric Agol and Levenberg-Marquardt least-squares minimization routine MPFITFUN by Craig Markwardt. P.M. and P.R.M. were supported by the Spitzer Science Center Grant C4030 to the Space Telescope Science Institute. A.B. was supported in part by NASA under grants NAG5-10760 and NNG04GL22G. This work is based on observations made with the Spitzer Space Telescope, which is operated by the Jet Propulsion Laboratory, California Institute of Technology under a contract with NASA. This publication also makes use of data products from the Two Micron All Sky Survey, which is a joint project of the University of Massachusetts and the Infrared Processing and Analysis Center/California Institute of Technology, funded by the National Aeronautics and Space Administration and the National Science Foundation. The authors would like to thank the reviewer Dr. Drake Deming for his helpful comments which have substantially improved the manuscript.

REFERENCES

- Barman, T. 2007, *ApJ*, 661, L191
 Burrows, A., Sudarsky, D., & Hubeny, I. 2006, *ApJ*, 650, 1140
 Burrows, A., Hubeny, I., Budaj, J., Knutson, H. A., & Charbonneau, D. 2007a, *ApJ*, 668, L171
 Burrows, A., Budaj, J., & Hubeny, I. 2007b, accepted to *ApJ*, ArXiv e-prints: arXiv:0709.4080
 Charbonneau, D., Brown, T. M., Noyes, R. W., & Gilliland, R. L. 2002, *ApJ*, 568, 377
 Charbonneau, D., et al. 2005, *ApJ*, 626, 523
 Charbonneau, D., Knutson, H. A., Barman, T., Allen, L. E., Mayor, M., Megeath, S. T., Queloz, D., & Udry, S. 2008, ArXiv e-prints, 802, arXiv:0802.0845
 Deming, D., Seager, S., Richardson, L. J., & Harrington, J. 2005, *Nature*, 434, 740
 Deming, D., Harrington, J., Seager, S., & Richardson, L. J. 2006, *ApJ*, 644, 560
 Deming, D., Harrington, J., Laughlin, G., Seager, S., Navarro, S. B., Bowman, W. C., & Horning, K. 2007, *ApJ*, 667, L199
 Fazio, G. G. et al. 2004, *ApJS*, 154, 10
 Fortney, J. J., Cooper, C. S., Showman, A. P., Marley, M. S., & Freedman, R. S. 2006, *ApJ*, 652, 746
 Fortney, J. J., & Marley, M. S. 2007, *ApJ*, 666, L45
 Fortney, J. J., Lodders, K., Marley, M. S., & Freedman, R. S. 2007, ArXiv e-prints, 710, arXiv:0710.2558
 Grillmair, C. J., Charbonneau, D., Burrows, A., Armus, L., Stauffer, J., Meadows, V., Van Cleve, J., & Levine, D. 2007, *ApJ*, 658, L115
 Harrington, J., Luszcz, S., Seager, S., Deming, D., & Richardson, L. J. 2007, *Nature*, 447, 691
 Holman, M. J., et al. 2006, *ApJ*, 652, 1715
 Hubeny, I., Burrows, A., & Sudarsky, D. 2003, *ApJ*, 594, 1011
 Knutson, H. A., et al. 2007a, *Nature*, 447, 183
 Knutson, H. A., Charbonneau, D., Allen, L. E., Burrows, A., & Megeath, S. T. 2008, *ApJ*, 673, 526
 Kopal, Z. 1959, *The International Astrophysics Series*, London: Chapman & Hall, 1959,
 Mandel, K., & Agol, E. 2002, *ApJ*, 580, L171
 Meixner, M., et al. 2006, *AJ*, 132, 2268
 McCullough, P. R., et al. 2006, *ApJ*, 648, 1228
 Morales-Calderón, M., et al. 2006, *ApJ*, 653, 1454
 Patten, B. M., Hora, J. L., Fazio, G. G., Barmby, P., Wang, Z., Makovoz, D. 2004, *Proc. SPIE*, 5487, 223
 Press, W. H., Teukolsky, S. A., Vetterling, W. T., & Flannery, B. P. 1992, *Cambridge: University Press*, —c1992, 2nd ed.,
 Richardson, L. J., Deming, D., Horning, K., Seager, S., & Harrington, J. 2007, *Nature*, 445, 892
 Swain, M. R., Vasisht, G., & Tinetti, G. 2008, *Nature*, 452, 32
 Tinetti, G., et al. 2007, *Nature*, 448, 169
 Torres, G., Winn, J. N., & Holman, M. J. 2008, ArXiv e-prints, 801, arXiv:0801.1841
 Werner, M. W., et al. 2004, *ApJS*, 154, 1
 Williams, P. K. G., Charbonneau, D., Cooper, C. S., Showman, A. P., & Fortney, J. J. 2006, *ApJ*, 649, 1020